Room Temperature Magnetic Rare-Earth Iron Garnet Thin Films with Ordered Mesoporous Structure

Christian Suchomski,[†,] Christian Reitz,[†] Celia T. Sousa,[‡] Joao P. Araujo,[‡] and Torsten Brezesinski[†,*]*

[†]Institute of Nanotechnology, Karlsruhe Institute of Technology, Hermann-von-Helmholtz-Platz 1, 76344 Eggenstein-Leopoldshafen, Germany, and [‡]Departamento de Fisica e Astronomia, Faculdade de Ciencias da Universidade do Porto and IFIMUP-IN, Rua do Campo Alegre 687, 4169-007 Porto, Portugal.

Abstract

Amphiphilic polymers are very attractive as porogens for the preparation of ordered mesoporous thin films and powders with pore sizes ranging from 40 down to a few nanometers in diameter because they are capable of both forming different superstructures and interacting with sol-gel precursors. In the present work, we report for the first time the synthesis of a series of highly crystalline rare-earth iron garnet ($RE_3Fe_5O_{12}$, RE = Y, Gd-Dy) thin films with cubic networks of interconnected pores averaging 17 nm in diameter through facile polymer templating of hydrated nitrate salts. Despite intricate crystallization pathways, e.g., $Y_3Fe_5O_{12}$ *via* $Y_4Fe_2O_9$ and *h*-$YFeO_3$, the nanoscale architecture of all these materials is only affected to a limited extent by solid-solid conversions at elevated temperatures. We specifically focus on the characterization of the morphology, microstructure and magnetic properties of polymer-templated $Y_3Fe_5O_{12}$. This novel mesoporous material is single phase after heating to 900 °C, free of major structural defects and is also well-defined on the atomic level, as evidenced by a combination of *in situ* and *ex situ* scattering/diffraction techniques, electron microscopy, Raman and X-ray photoelectron spectroscopy and time-of-flight secondary ion mass spectrometry. The high quality of the nanocrystalline $Y_3Fe_5O_{12}$ thin films with overall soft magnetic-like characteristics and moderate anisotropy is further confirmed by SQUID magnetometry measurements. The magnetization behavior in the temperature range 5–380 K well describes Bloch's $T^{3/2}$ law for a 3D Heisenberg-type ferromagnet.

Keywords

rare-earth iron garnet, self-assembly, mesoporous, nanocrystalline, Heisenberg ferromagnet, Bloch’s $T^{3/2}$ law

Introduction

Both soft and hard magnetic metal oxides are of interest to researchers from a wide range of disciplines, including information technology, biomedicine and so forth.[1-3] In recent years, it has been shown that magnetic properties such as coercivity, H_C, and saturation magnetization, M_{Sat}, can be tailored by changing the material morphology and microstructure (i.e., increasing/decreasing magnetocrystalline, shape or strain anisotropy) and by reducing the grain size (i.e., finite size and surface effects, including spin canting/freezing etc.).[4-8] This has renewed the interest in magnetic metal oxides of all kinds, in particular nanocrystalline forms of these materials.

Coupling forces between the magnetic dipoles of neighboring atoms distinguish ferromagnetic from paramagnetic materials. Bulk (microcrystalline) ferromagnetics typically consist of a large number of Weiss domains with uniform magnetization separated by so-called domain walls. At temperatures above the Curie temperature, T_C, the thermal energy, k_BT, is sufficient to overcome the coupling forces so that the material becomes thermally unstable and exhibits paramagnetic behavior.[9] Superparamagnetism often observed in sub-20 nm single domain particles is different in that the material experiences random thermal fluctuations already at temperatures below T_C.[10]

In this work, the sol-gel synthesis of a series of large-pore mesoporous rare-earth iron garnet thin films through polymer templating of hydrated nitrate salt precursors is reported. We specifically focus on yttrium iron garnet, $Y_3Fe_5O_{12}$, a ternary oxide that, as we show here, can be produced with highly crystalline walls while preserving both the pore structure – despite solid-solid conversions throughout the course of thermal annealing – and the magnetic dipolar coupling observed in the bulk.

Yttrium iron garnet, also referred to as YIG, has many technologically significant properties. For example, microcrystalline YIG shows ferrimagnetic behavior at room temperature, has a high electrical resistance and further exhibits interesting magneto-optical properties such as large Faraday rotation.[11-13] As a result, this synthetic garnet finds widespread use in microwave, data storage, magneto-optical and other applications.[13-15] YIG was first prepared by Bertaut and Forrat in 1956 and is a prototype

compound of the ferrimagnetic iron garnet class with space group $Ia\bar{3}d$ (O_h^{10}), in which Fe^{3+} ions are coupled *via* antiferromagnetic superexchange interactions.[16,17] The synthesis of purely cubic YIG has proven to be challenging in practice. This is due in part to the fact that orthorhombic yttrium orthoferrite, *o*-$YFeO_3$, is formed as an intermediate during conventional solid-state reaction.[18] Therefore, temperatures well above 1000 °C are typically required to obtain single phase material.[19,20] However, prolonged annealing at such high temperatures leads to microcrystalline YIG. It has been shown, nevertheless, that both the annealing time and temperature can be significantly lowered by using synthetic routes other than solid-state reaction, including sol-gel[21,22], auto-combustion[23,24] and co-precipitation[19,25]. These methods have been successfully applied to the preparation of nanocrystalline YIG. While the fabrication of nanocoatings and nanopowders through wet chemical processes has already been reported in the literature, the use of evaporation-induced self-assembly (EISA)[26-28] to achieve mesoporous forms of this material and other related rare-earth iron garnets has not yet been described.

Polymer templating of inorganic materials can be used to produce oxide ceramics with different pore structures such as cubic and 2D-hexagonal.[29-34] Their formation relies on the solution-phase coassembly of either molecular or nanocrystal building blocks with a polymer structure-directing agent.[33-39] However, the preparation of ternary or even more complex metal oxides from sol-gel precursors is complicated and, thus, literature reports on such mesoporous materials are scarce. Part of the reason for this is the difficulty of controlling the amorphous-to-crystalline conversion at elevated temperatures. Many polymer-templated materials accommodate walls that are not sufficiently thick to allow for uniform crystallization while retaining the nanoscale structure.

Here, we take advantage of the superior templating properties of a poly(ethylene-*co*-butylene)-*block*-poly(ethylene oxide)[31,38,40,41] diblock copolymer to synthesize to our knowledge for the first time single phase rare-earth iron garnets with a well-defined mesoporous morphology. This polymer has been proven in the past to be well suited for use as a structure-directing agent for preparing ordered large-pore mesoporous thin films and powders with nanocrystalline walls.[31,38,41-43] In addition to the

synthesis of the different rare-earth iron garnets and the characterization of the porous properties and the microstructure, we show that polymer-templated YIG thin films exhibit soft magnetic behavior with narrow hysteresis loops somewhat similar to that observed in the bulk. Furthermore, we demonstrate that the magnetic moment varies as $T^{3/2}$ over a broad temperature range, in agreement with Bloch's prediction for a 3D Heisenberg-type ferromagnet. Overall, we believe that these novel mesoporous materials are particularly interesting for room temperature nanomagnetic host/guest applications.

Experimental Section

Materials. $Fe(NO_3)_3 \cdot 9H_2O$ (99.99%), $Y(NO_3)_3 \cdot 6H_2O$ (99.99%), $Gd(NO_3)_3 \cdot 6H_2O$ (99.99%), $Tb(NO_3)_3 \cdot 6H_2O$ (99.99%), $Dy(NO_3)_3 \cdot 6H_2O$ (99.99%) and 2-methoxyethanol (99.8%) were purchased from Sigma-Aldrich. $H[(CH_2CH_2)_{0.67}(CH_2CHCH_2CH_3)_{0.33}]_{89}(OCH_2CH_2)_{79}OH$, also referred to as KLE[40,44], was used as polymer structure-directing agent.

Synthesis. Both hydrated metal nitrate salt precursors and 40 mg of KLE are dissolved in a mixed solvent of 0.6 mL of 2-methoxyethanol and 1.6 mL of absolute ethanol. Table 1 summarizes reagent masses for each type of thin film prepared in this work. Once the solution is clear, thin films can be produced *via* dip-coating on virtually any polar substrate. Optimal conditions include relative humidities of 10-15% and constant withdrawal rates of 5-10 $mm \cdot s^{-1}$. After a drying time of 3-4 min, the samples are directly transferred to an oven at 80 °C for 12 h and then heated to 300 °C using a 44 min ramp followed by aging for 6 h (nonporous powder material was prepared under identical conditions but without any KLE polymer and 2-methoxyethanol). Lastly, the films are heated to temperatures ranging between 830 °C and 900 °C in air at a rate of 10 $°C \cdot min^{-1}$ both to remove the KLE polymer and to crystallize the amorphous wall structure.

Table 1. Recipes for the synthesis of $Y_3Fe_5O_{12}$, $Gd_3Fe_5O_{12}$, $Tb_3Fe_5O_{12}$ and $Dy_3Fe_5O_{12}$ thin films.

	$Y(NO_3)_3 \cdot 6H_2O$ (mg)	$Gd(NO_3)_3 \cdot 6H_2O$ (mg)	$Tb(NO_3)_3 \cdot 6H_2O$ (mg)	$Dy(NO_3)_3 \cdot 6H_2O$ (mg)	$Fe(NO_3)_3 \cdot 9H_2O$ (mg)
$Y_3Fe_5O_{12}$	140.1	–	–	–	246.4
$Gd_3Fe_5O_{12}$	–	134.1	–	–	200.0
$Tb_3Fe_5O_{12}$	–	–	133.9	–	199.0
$Dy_3Fe_5O_{12}$	–	–	–	133.3	196.5

Methods. Bright-field transmission electron microscopy (TEM) and scanning electron microscopy (SEM) images were taken with a CM30-ST from Philips and a MERLIN from Carl Zeiss, respectively. X-ray diffraction (XRD) measurements were carried out on an X'Pert PRO diffractometer from PANalytical instruments. Grazing incidence small-angle X-ray scattering (GISAXS) patterns were collected at the German synchrotron radiation facility HASYLAB at DESY on beamline BW4 using a sample-detector distance of approx. 1820 mm. X-ray photoelectron spectroscopy (XPS) data were acquired on a Physical Electronics ESCA 5600 spectrometer with monochromatic Al-Kα X-ray source and a multichannel detector OmniIV. The electron takeoff angle to the sample surface was adjusted to 50°. The C 1*s* signal from adventitious hydrocarbon at 284.8 eV was used as energy reference to correct for charging. The samples were also analyzed by time-of-flight secondary ion mass spectrometry (TOF-SIMS) using a TOF-SIMS 5 from ION-TOF GmbH. A primary ion beam of 25 keV Bi^+ was used to generate secondary ions. Sputter etching was carried out using a beam of 1 keV O^+ (I_0 = 131.1 nA). Raman spectra were acquired using the SENTERRA dispersive Raman microscope from Bruker Optics equipped with an objective from Olympus (MPlan N 50x, FN = 22, NA = 0.40) and a Nd:YAG laser (λ = 532 nm, P = 2 mW). N_2-physisorption measurements were conducted at 77 K on (550 ± 20) nm thick YIG films with a total area of approx. 55 cm^2 using the Autosorb-1-MP automated gas adsorption station from Quantachrome Corporation (error margin: ±5%). Optical absorption measurements were carried out on a Perkin Elmer Lambda 900 UV-vis-NIR spectrophotometer. A substrate made from fused silica and an aluminum mirror served as a reference for transmission and reflection measurements, respectively. Thermogravimetric analysis (TGA) data were obtained with a Netzsch STA 409 PC. The

thermobalance was coupled to a Balzers QMG 421 quadrupole mass spectrometer. The ionization energy was 70 eV. The film thickness was determined with an Alpha Step IQ Surface Profiler from KLA Tencor. For crystal structure visualization, the software Crystal Impact Diamond version 3.2i was used. Magnetic susceptibility measurements were carried out on a Quantum Design superconducting quantum interference device (SQUID) magnetometer for the temperature range of 5–380 K in magnetic fields up to ±50 kOe.

Results and Discussion

The mesoporous rare-earth iron garnet thin films studied in this work were prepared by solution-phase coassembly of hydrated metal nitrate salts with a poly(ethylene-*co*-butylene)-*block*-poly(ethylene oxide) diblock copolymer, also referred to as KLE. In short, in a typical synthesis both the inorganic precursors and the diblock copolymer are dissolved in a mixed solvent of ethanol and 2-methoxyethanol. Once the solution is clear, high-quality, large-area films with thicknesses ranging from a few nanometers to several hundreds of nanometers can be produced *via* facile dip-coating on partially oxidized Si(100) wafers, quartz glass slides and other polar substrates. Thermal treatment can then be used to drive condensation, combust the polymer and to induce crystallization of the glassy wall structure.

Following our previous work on KLE-templated metal oxides,[31,41-43] here, we also take advantage of the superior templating properties of this amphiphilic polymer to achieve for the first time single phase rare-earth iron garnets with a cubic pore-solid architecture. Unlike the triblock copolymers of the Pluronic family, KLE has proven highly efficient for the preparation of non-silicate mesostructured materials with nanocrystalline walls. This is due in part to the fact that KLE produces materials with fairly thick walls that are capable of accommodating crystallites larger than 15 nm in diameter.

To obtain insight into the nanoscale structure of the mesoporous rare-earth iron garnet thin films, a series of scanning electron microscopy (SEM), transmission electron microscopy (TEM), *in situ* small-angle X-ray scattering (SAXS) and *ex situ* grazing incidence small-angle X-ray scattering (GISAXS) measurements was carried out. **Figure 1** shows both top view and cross-sectional SEM images and

bright-field TEM images of an approx. 400 nm thick YIG film after removal of the KLE polymer and crystallization at 900 °C. The top view SEM image reveals a distorted but macroscopically homogeneous network of pores averaging 16 nm in diameter and further indicates that the sample is crack-free on the micrometer level and that the pore cavities at the solid-air interface are open (see also SEM and TEM images in **Figure S1** in ESI). Cross-sectional SEM establishes that the nanoscale structure persists throughout the bulk of the films. The TEM imaging data are consistent with the SEM observations in that they show a cubic network of slightly deformed pores that are surrounded by nanocrystalline grains. The result that the wall structure is highly crystalline after heating films to 900 °C is also confirmed by selected-area electron diffraction (SAED). The pattern in the inset of panel (d) shows Debye-Scherrer rings typical of a material with randomly oriented grains. The *d*-values of the reflections are in good agreement with those obtained from the JCPDS (Joint Committee on Powder Diffraction Standards) reference card no. 43-0507 for cubic YIG with space group $Ia\bar{3}d$ (O_h^{10}).

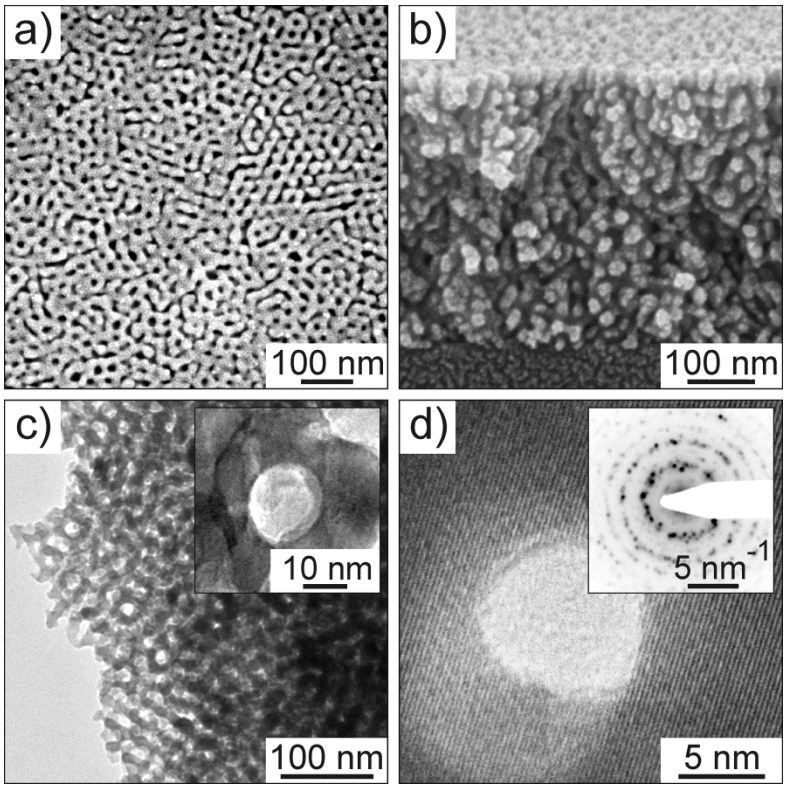

Figure 1. Microstructure of KLE-templated $Y_3Fe_5O_{12}$ thin films heated to 900 °C. (a) Top view SEM image showing a distorted cubic network of 16 nm diameter pores at the air-solid interface. (b) Cross-sectional SEM image. (c) Bright-field TEM images at different magnifications. (d) High-resolution

TEM image showing the (420) lattice planes of cubic $Y_3Fe_5O_{12}$. The inset in panel (d) is an SAED pattern.

Similar microstructure data are obtained for KLE-templated $Gd_3Fe_5O_{12}$, $Tb_3Fe_5O_{12}$ and $Dy_3Fe_5O_{12}$ thin films. **Figure 2** shows SEM images of the top surface and bright-field TEM images of the interior of all three materials at different magnifications, which indicate that they also exhibit a defined porosity after crystallization at temperatures above 800 °C in air (see also low-magnification SEM images in **Figure S2** in ESI). Similar to KLE-templated YIG, the average lateral pore sizes are 17 nm in diameter. From these images, it seems likely that the grains have an anisotropic shape. This would help explain the formation of thin films with mesoporous morphologies partially reminiscent of more worm-like structures. Both SAED and high-resolution TEM establish that the different rare-earth iron garnets in fact are highly crystalline and that the presence of mesopore cavities only interferes to a limited extent with the crystallization. However, at first glance the pore ordering of these materials seems slightly less than that observed for YIG.

Overall, the results with SEM and TEM lead us to conclude that $Y_3Fe_5O_{12}$, $Gd_3Fe_5O_{12}$, $Tb_3Fe_5O_{12}$ and $Dy_3Fe_5O_{12}$ can be templated using the large diblock copolymer KLE to produce high-quality thin films with a distorted cubic network of pores. These oxide materials not only have a thermally stable and robust framework but are also free from major structural defects despite the fact that they undergo solid-solid conversions throughout the course of crystallization (see section on X-ray diffraction below).

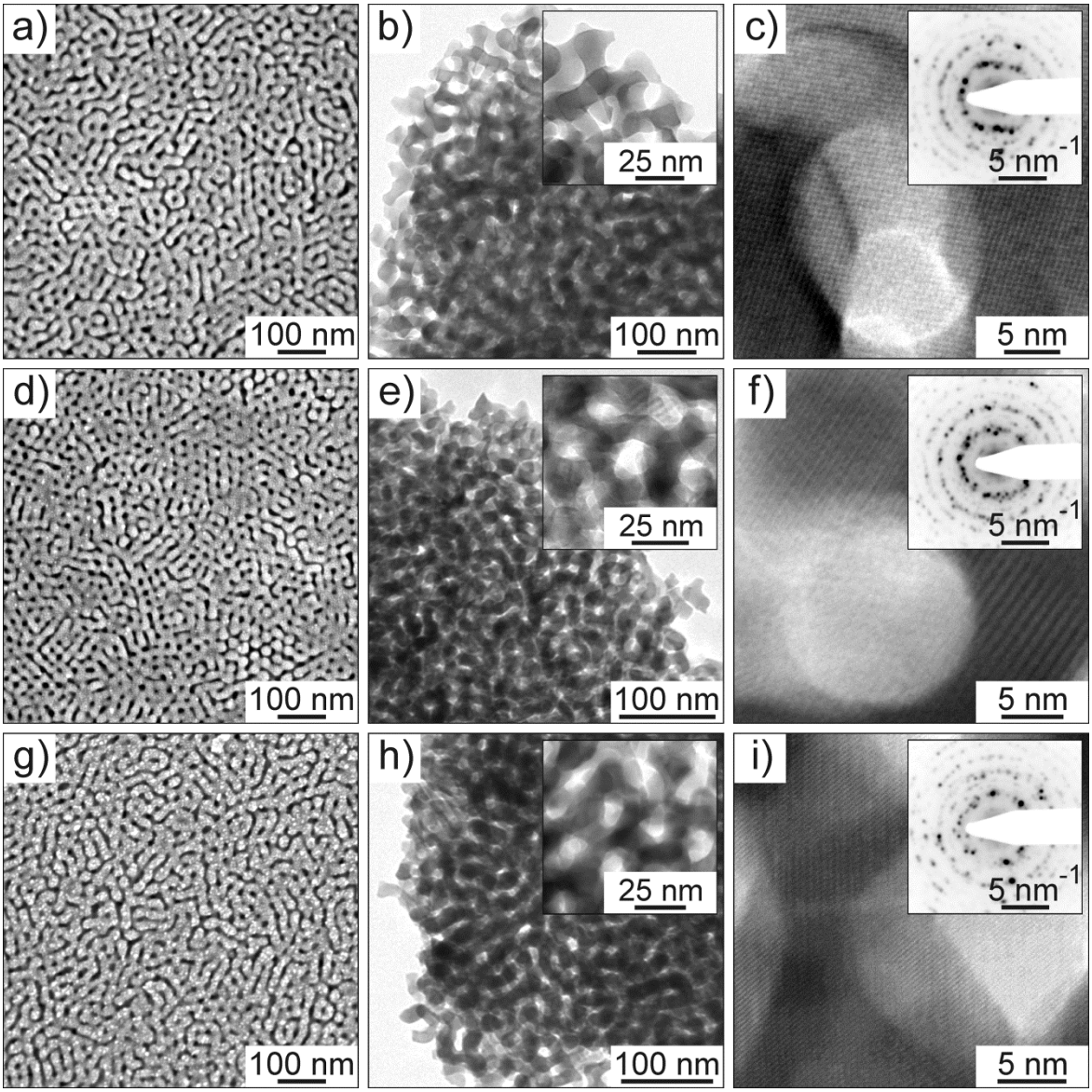

Figure 2. Microstructure of KLE-templated $Gd_3Fe_5O_{12}$ (a–c), $Tb_3Fe_5O_{12}$ (d–f) and $Dy_3Fe_5O_{12}$ (g–i) thin films heated to 830 °C, 840 °C and 850 °C, respectively. (a, d, g) Top view SEM images. (b, e, h) Bright-field TEM images at different magnifications. (c, f, i) High-resolution TEM images and SAED patterns (insets) showing the pore walls to be highly crystalline.

The film formation after dip-coating and the effect that network condensation and crystallization has on the pore structure was studied by synchrotron-based *in situ* SAXS and *ex situ* GISAXS, respectively. **Figure 3** shows typical SAXS patterns as a function of drying time for KLE-templated YIG thin films (see also scheme of the experimental setup in **Figure S3** in ESI). From these data, it is evident that the

mesophase forms rather slowly. This result is not very surprising, however, and can be explained by the fact that a mixed solvent of ethanol and 2-methoxyethanol was used in the synthesis. We note that previous works on mesoporous metal oxide thin films produced from precursor solutions containing 2-methoxyethanol have shown that it helps obtain materials with a periodic nanoscale structure and a stronger preferred orientation of the mesophase relative to the substrate.[43,45] Part of the reason for this is that the deposited samples remain in a quasi-fluid state for a longer time during the coassembly process. Furthermore, it can be seen that the YIG thin films exhibit a face-centered cubic (*fcc*) structure with (111) orientation and lattice parameter, *a*, of 40 nm and that the mesophase formation is fully completed after approx. 180 s. Thereafter, the films can be directly transferred to an oven at 80 °C to drive condensation in order to stabilize the framework. Overall, *in situ* SAXS shows that sufficient drying time must be allowed prior to thermal treatment to ensure that a well-defined pore-solid architecture is obtained after removal of the polymer structure-directing agent at elevated temperatures.

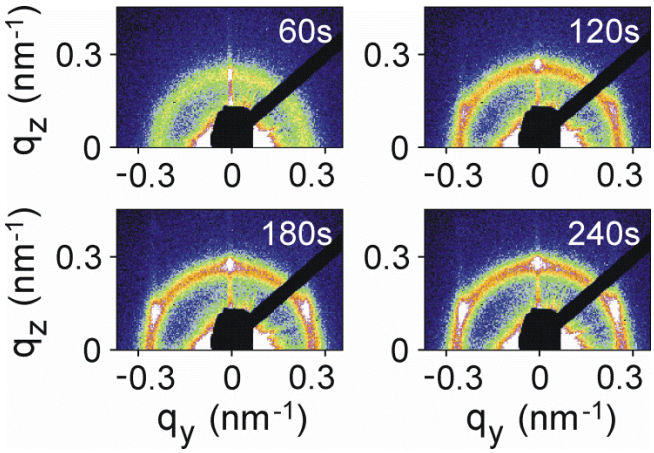

Figure 3. *In situ* SAXS patterns at an angle of incidence $\beta = 5°$ obtained on a KLE-templated $Y_3Fe_5O_{12}$ thin film as a function of drying time.

Figure 4 shows *ex situ* GISAXS patterns at an angle of incidence $\beta = 0.2°$ obtained on KLE-templated $Y_3Fe_5O_{12}$, $Gd_3Fe_5O_{12}$, $Tb_3Fe_5O_{12}$ and $Dy_3Fe_5O_{12}$ thin films with both amorphous and crystalline walls. Amorphous samples produce patterns with distinct maxima. These maxima are characteristic of a 3D pore structure with cubic symmetry. From the same GISAXS patterns, it can also

be seen that the intensity of the scattering maxima in the *z*-direction is much weaker than that of the other reflections. This is particularly evident for $Y_3Fe_5O_{12}$ and $Gd_3Fe_5O_{12}$. However, the lack of strong scattering does not necessarily indicate a lack of periodicity but is rather a result of the morphological anisotropy of the films – changes in nanoscale structure due to pore transformation from spherical to oblate during volume contraction have a much greater impact on the out-of-plane periodicity. We note that this kind of pore flexing cannot take place in-plane because the films are bound to the substrate. Consequently, the in-plane contraction is negligible. Heating the amorphous films to temperatures above 600 °C does not lead to further contraction because the materials are virtually fully crosslinked after aging at 300 °C. This result is also confirmed by thermogravimetric analysis-mass spectrometry (TGA-MS, see **Figure 5a**). The data in **Figure 4** further show that crystalline samples have completely lost the scattering in the *z*-direction. The reason for this loss can be attributed to changes in nanoscale structure during conversion of the initially amorphous materials. In addition, the appearance of in-plane maxima at lower ***q***-values can be observed. These maxima are much more pronounced for $Tb_3Fe_5O_{12}$ and $Dy_3Fe_5O_{12}$ and indicate that the crystallization process is associated with partial restructuring of the cubic mesoporous thin films. This structural transformation toward more disorder (i.e., worm-like structures) is likely a result of the fact that several metastable intermediates are formed before single phase rare-earth iron garnets are achieved. However, the GISAXS results corroborate the electron microscopy data and provide ample evidence that the sol-gel derived materials can be crystallized with retention of the pore network.

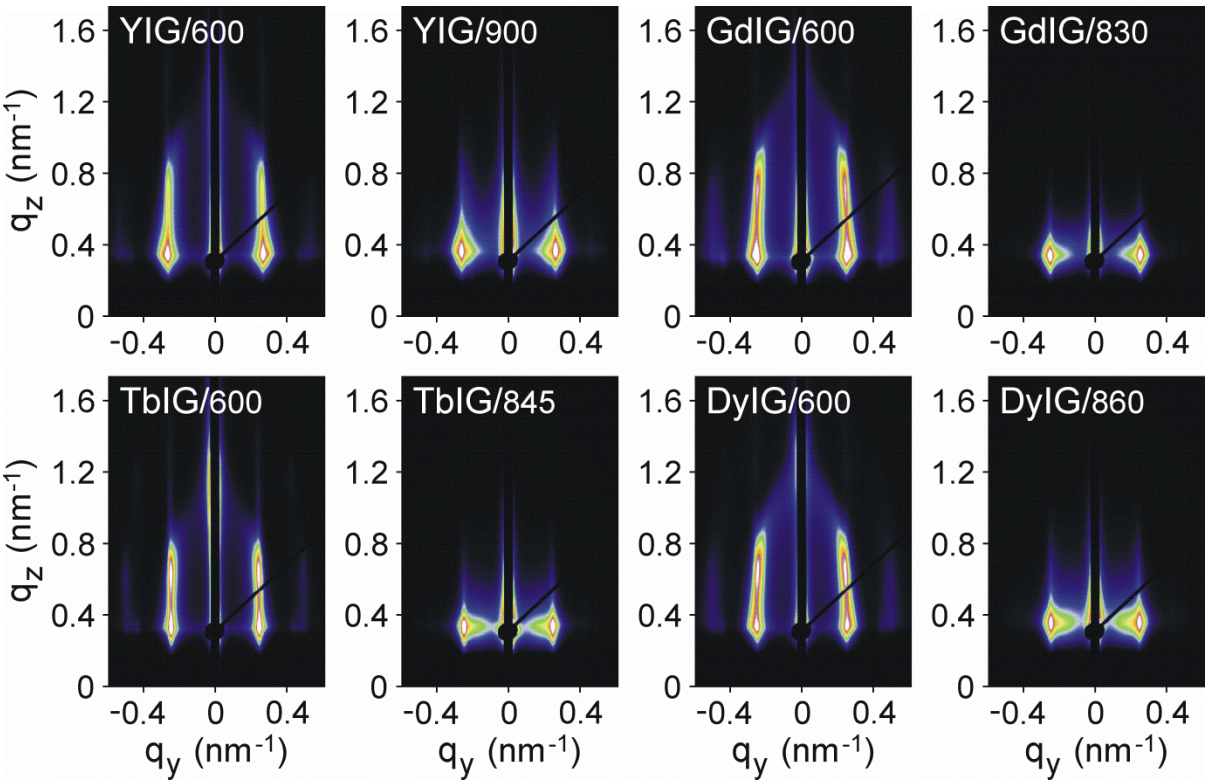

Figure 4. *Ex situ* GISAXS patterns at an angle of incidence β = 0.2° obtained on KLE-templated $Y_3Fe_5O_{12}$ (YIG), $Gd_3Fe_5O_{12}$ (GdIG), $Tb_3Fe_5O_{12}$ (TbIG) and $Dy_3Fe_5O_{12}$ (DyIG) thin films. The acronyms on the top left corner of each panel represent both the rare-earth iron garnet from which the data were collected and the corresponding annealing temperature.

In the following sections, we specifically focus on both the microstructure and physical properties of mesoporous YIG. A comparative study of the other rare-earth iron garnets shown here will be presented in a separate work.

As mentioned above, TGA-MS studies were carried out to obtain insight into the formation of glassy $RE_3Fe_5O_x$ prior to crystallization. For these experiments, powder material was produced without any KLE polymer and 2-methoxyethanol but under otherwise identical conditions. The data in panels (a) and (b) of **Figure 5** indicate a mass loss of 52% by 900 °C and further show that the hydrated nitrate salts used to produce the films begin to decompose at temperatures above 60 °C. This process is virtually completed after aging at 300 °C. Both $Fe(NO_3)_3{\cdot}9H_2O$ and $Y(NO_3)_3{\cdot}6H_2O$ first dissolve in their

own water of crystallization followed by hydrolysis and dehydration.[46] According to literature reports on related nitrate salts, the latter reactions are associated with formation of hydroxy nitrate species. Thereafter, the hydroxyl and nitrate groups decompose to H_2O and NO_x in several steps. The small mass loss at temperatures above 300 °C is likely because of decomposition of *in situ* generated yttrium oxynitrate species, $YO_x(NO_3)_y$.[47,48] Such compounds have been shown to be thermally quite stable.[49] Lastly, we note that the discrepancy between measured and theoretical mass loss (52% versus 76%) is related to the procedure of making the powder starting material (see Experimental section), which already induced partial dehydration and hydrolysis of both molecular precursors. Nevertheless, TGA-MS verifies that different ferric and yttrium hydroxy- and oxynitrate species are formed during thermal treatment, which then convert to glassy $Y_3Fe_5O_x$ at moderate temperatures.

The porous properties of the KLE-templated YIG thin films were also analyzed by N_2-physisorption at 77 K. **Figure 5c** shows typical type-IV adsorption/desorption isotherms for (550 ± 20) nm thick films with a total area of approx. 55 cm^2 heated to 800 °C and 900 °C. As expected, higher annealing temperatures lead to a reduction in both pore volume and specific surface area. This is due to the onset of crystallization, which is at $\vartheta \approx 800$ °C (see section on X-ray diffraction below). The crystallization process and the associated changes in pore size and shape are most likely also responsible for the shift of the lower hysteresis closure point because the pore geometry is known to have a profound effect on the desorption properties. Using a cross-sectional area of 16.2 $Å^2$ for N_2, Brunauer-Emmett-Teller (BET) surface areas of 300 $m^2 \cdot cm^{-3}$ and 150 $m^2 \cdot cm^{-3}$ and porosities of 50% and 42% are obtained for samples heated to 800 °C and 900 °C, respectively. These results are in fair agreement with other KLE-templated oxide materials of similar structure and further provide evidence for the accessibility of pore cavities in the interior of the films.

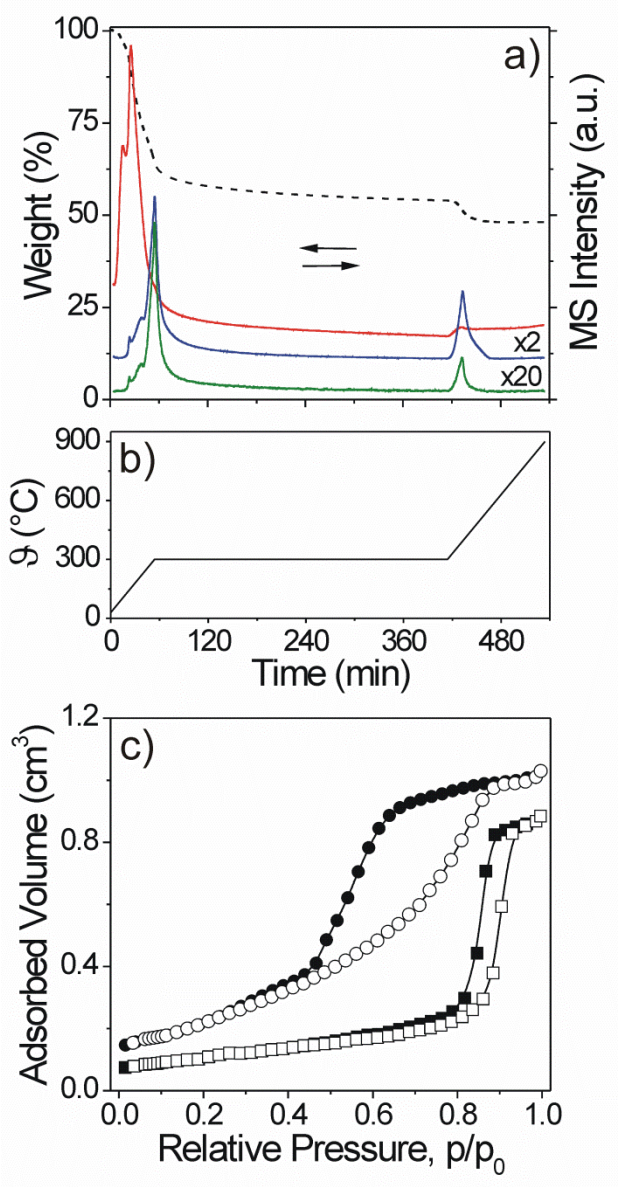

Figure 5. (a) TGA-MS data for a mixture of hydrated ferric and yttrium nitrate salt precursors measured in synthetic air in the temperature range between 30 °C and 900 °C. The dashed line represents the TGA curve. The MS analysis shows H_2O (m/e = 18) in red, NO (m/e = 30) in blue and NO_2 (m/e = 46) in green. (b) Scheme of the heating profile. (c) N_2-adsorption/desorption isotherms obtained on (550 ± 20) nm thick mesoporous YIG films with a total area of approx. 55 cm^2 heated to 800 °C (○) and 900 °C (□).

YIG crystallizes in a body-centered-cubic (*bcc*) structure with space group $Ia\bar{3}d$ (O_h^{10}).[17,50] The unit cell consists of 160 atoms, i.e., eight formula units $Y_3Fe_5O_{12}$ (see **Figure 6)**. In this structure, non-

magnetic Y^{3+} ions ([Kr] $4d^0 5s^0$) are located on the dodecahedral 24(*c*) sites (Wyckoff notation) while magnetic Fe^{3+} ions ([Ar] $3d^5 4s^0$) occupy the tetrahedral 24(*d*) sites and the octahedral 16(*a*) sites in a ratio of 3:2. Because the Fe^{3+} ions sit on crystallographically non-equivalent sites, they form two different magnetic sublattices with antiferromagnetic $Fe^{3+}_{tet}(\downarrow) - O - Fe^{3+}_{oct}(\uparrow)$ interactions leading to spontaneous magnetization. The strength of this negative superexchange interaction has been shown to strongly depend on the bond angle and length and the temperature.[17]

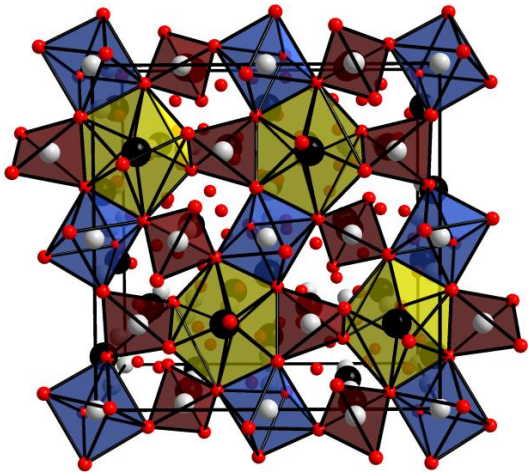

Figure 6. Unit cell for cubic YIG. Yttrium atoms occupying the dodecahedral 24(*c*) sites are shown in black, iron atoms on both the octahedral 16(*a*) and tetrahedral 24(*d*) sites in white and oxygen atoms on the 96(*h*) sites in red. The different coordination spheres are indicated by colored polyhedra.

To obtain a more complete picture of the mesoporous material, a series of UV-vis spectroscopy, X-ray diffraction (XRD), time-of-flight secondary ion mass spectrometry (TOF-SIMS) as well as Raman and X-ray photoelectron spectroscopy (XPS) measurements were carried out. **Figure 7** shows plots for both direct and indirect optical transitions in KLE-templated YIG thin films heated to 900 °C. Such samples reveal a deep yellow color at room temperature. This differs from bulk forms of YIG, which have been shown to have more of a dark green color. In the wavelength range between 800 nm and 400 nm (see absorbance spectrum in **Figure S4** in ESI) we find overall seven absorption bands at approx. 689 nm (~1.80 eV), 620 nm (~2.00 eV), 503 nm (~2.47 eV), 487 nm (~2.55 eV), 470 nm (~2.64 eV), 447 nm

(~2.77 eV) and 413 nm (~3.02 eV). These bands presumably stem from crystal field *d-d* transitions involving high-spin Fe^{3+} ions on both the tetrahedral and octahedral sites.[51,52] However, density functional theory (DFT) calculations by Ching *et al*. do not support the appearance of such transitions as they are generally spin forbidden.[53] Nevertheless, it has been shown that in some iron oxides, including $LiFe_5O_8$[54] and $GaFeO_3$[55], apparently forbidden crystal field *d-d* transitions may become allowed through antiferromagnetic spin coupling between next-nearest neighbor Fe atoms.[56] According to literature reports, absorption bands at wavelengths below 413 nm can be ascribed to both oxygen-to-iron and oxygen-to-yttrium charge transfer (CT) as well as intervalence transitions between Fe^{3+} ions on the tetrahedral and octahedral sites.[57-59] The optical band gap at room temperature was found to lie in the range 2.6 eV to 2.9 eV and has been shown to arise due to excitation from O 2*p* valence band to Fe_{oct} 3*d* conduction band.[60-62] For this reason, YIG is referred to as a charge-transfer insulator. We estimate the band gap energy, E_g, from the data for a direct transition as being (2.84 ± 0.05) eV – the lack of the characteristic shape of the plot $\alpha^{1/2}$ versus photon energy argues against an indirect optical transition in the KLE-templated YIG thin films. This value is close to the measured E_g and is further also in fair agreement with the theoretical value of 2.66 eV reported by Ching *et al*.[53] The slight blue-shift is not surprising because the material employed in this work is nanocrystalline and, thus, such shift may be expected.

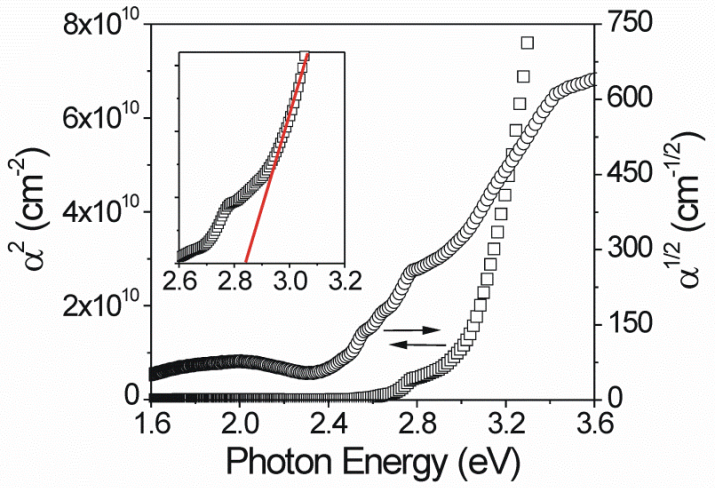

Figure 7. Direct (□) and indirect (○) optical transitions in KLE-templated YIG thin films heated to 900 °C. The intercept of the red line with the abscissa in the inset yields the direct band gap energy, E_g.

Both the crystallization behavior and pathway were investigated by XRD and Raman spectroscopy. **Figure 8a** shows typical XRD patterns for KLE-templated YIG thin films heated to 800 °C, 850 °C and 900 °C. It can be clearly seen that the crystallization process begins at temperatures equal to or lower than 800 °C and that several metastable phases are formed during continuous heating. Single phase YIG is obtained at 900 °C if a heating rate of 10 °C·min^{-1} is used. The average grain size was determined by applying the Scherrer equation to the line broadening of the most intense peaks labeled in **Figure 8a**. This analysis provides a value of 29 nm, which implies that a single nanocrystal forms the wall over a distance encompassing more than one pore cavity. The presence of larger amounts of binary oxides such as α-Fe_2O_3 and *C*-type Y_2O_3 due to nanoscale phase separation can be ruled out on the basis of the XRD data.

In the pseudo-binary Y_2O_3-Fe_2O_3 system, only orthorhombic yttrium orthoferrite, *o*-$YFeO_3$, with space group *Pnma* (D_{2h}^{16}) is known in addition to the thermodynamically stable garnet phase.[63-65] However, in recent years it has been shown that yttrium orthoferrite can also crystallize with hexagonal symmetry (space group $P6_3/mmc$ (D_{6h}^{4})).[66,67] A comparison with data reported in the literature shows that the broad peaks at 2θ = 30.8° (004) and 33.5° (102) in fact belong to metastable *h*-$YFeO_3$,[68] which does not transform into the orthorhombic perovskite polymorph at temperatures above 850 °C (see also Raman spectroscopy below). Furthermore, we find another nanocrystalline intermediate in the temperature range between 800 °C and 850 °C. The XRD peaks at 2θ = 28.7°, 30.2°, 33.8° and 35.3° match those of monoclinic $RE_4Ga_2O_9$ (RE = Y, Nd, Sm) with space group $P2_1/c$ (C_{2h}^{5}).[69,70] Because the ionic radii of trivalent iron and gallium are virtually identical, we expect very similar XRD patterns for the gallium and iron compounds. Also, Popova *et al.* have shown that $Y_4Ga_2O_9$ only exists in a narrow temperature interval in the Y_2O_3-Ga_2O_3 system.[69] This result is in agreement with our data. We

therefore assume that $Y_4Fe_2O_9$, which has not yet been described in the literature, is formed as an intermediate in the synthesis. Lastly, we note that the presence of Y_3FeO_6 can be ruled out. A series of RE_3FeO_6 (RE = La, Nd, Sm, Eu, Gd) compounds has recently been produced using the hydroxide flux method.[71] These materials adopt an orthorhombic structure with space group $Cmc2_1$ (C_{2v}^{12}) and are isotypic to the corresponding rare-earth gallates, RE_3GaO_6 (Ln = Nd-Er, Y).[72,73] Overall, the KLE-templated YIG thin films reveal an intricate crystallization pathway which is somewhat similar to that observed for yttrium aluminum garnet, $Y_3Al_5O_{12}$ (YAG), showing the same intermediates.[74,75] However, the most remarkable result is, perhaps, that the nanoscale structure is only affected to a limited extent by the different solid-solid conversions, which emphasizes the robustness of the mesoporous framework.

The TOF-SIMS profile of an approx. 200 nm thick KLE-templated YIG film with nanocrystalline walls in **Figure 8b** illustrates the distribution of Fe^+, Y^+ and C^+ as a function of depth from the top surface. These data establish that both the Fe^{3+} and Y^{3+} ions are homogeneously distributed throughout the films. In addition, it is apparent that the KLE polymer is fully removed after heating films to 900 °C. Only minor amounts of hydrocarbons can be detected at the sample/air interface, which is in agreement with the result from XPS (see **Figure 10** below).

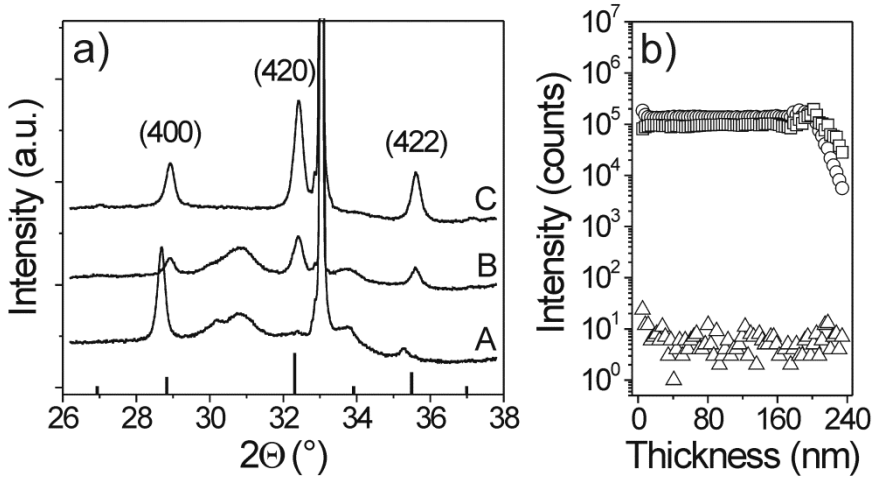

Figure 8. (a) XRD patterns of KLE-templated YIG thin films heated to 800 °C (A), 850 °C (B) and 900 °C (C). It should be noted that only the most intense peaks are indexed. The line pattern in panel (a) represents JCPDS reference card no. 43-0507 for cubic YIG. (b) TOF-SIMS profile of an approx. 200

nm thick KLE-templated YIG film heated to 900 °C showing the distribution of Fe^+ (○), Y^+ (□) and C^+ (△) as a function of depth from the top surface.

Because Raman spectroscopy is more sensitive to small amounts of second phases and intrinsic defects than conventional XRD techniques, a series of such measurements was made for KLE-templated YIG thin films on both partially oxidized Si(100) wafers and quartz glass slides. Typical Raman spectra are shown in panels (a) and (b) of **Figure 9**. According to group theory, defect-free YIG has 25 first-order Raman-modes (namely $3\times A_{1g}$, $8\times E_g$ and $14\times T_{2g}$ modes).[76] Overall, we can see 15 bands in the frequency range between 100 cm^{-1} and 750 cm^{-1}. **Table 1** summarizes the peak frequencies and Raman band assignments for both KLE-templated thin films heated to 900 °C and single crystals of YIG[77] (Song *et al*). Our data are in fair agreement with those obtained on the single crystals. The absence of a few bands in the high-frequency region can be attributed to line broadening because of finite size effects (phonon confinement) and superposition of the spectra from the substrate. We also note that some have very similar peak frequencies and, thus, they can only be distinguished by means of polarized Raman scattering. Apart from the Raman modes predicted by group theory, we find a comparatively weak shoulder band at ~286 cm^{-1}, which was not observed in the single crystals.[77,78] This band is also present in the spectrum for non-templated YIG powder material (see also XRD pattern in **Figure S5**), as shown in **Figure 9a**, and is presumably associated with some kind of cation disorder (so-called antisite defects). For example, it has been demonstrated by solid-state NMR and EXAFS spectroscopy that minor amounts of Y^{3+} ions (radius ~1.01 Å) on dodecahedral sites and Fe^{3+} ions (radius ~0.64 Å) on octahedral sites can exchange places with each other.[79,80] As a result, non-defect-free YIG might show more than the 25 Raman modes predicted by group theory. Considering the fact that the nanocrystalline thin films studied here are solution processed *via* sol-gel methods, they are expected to show signs of disorder. More importantly, however, the presence of impurity phases in samples heated to 900 °C can indeed be ruled out.

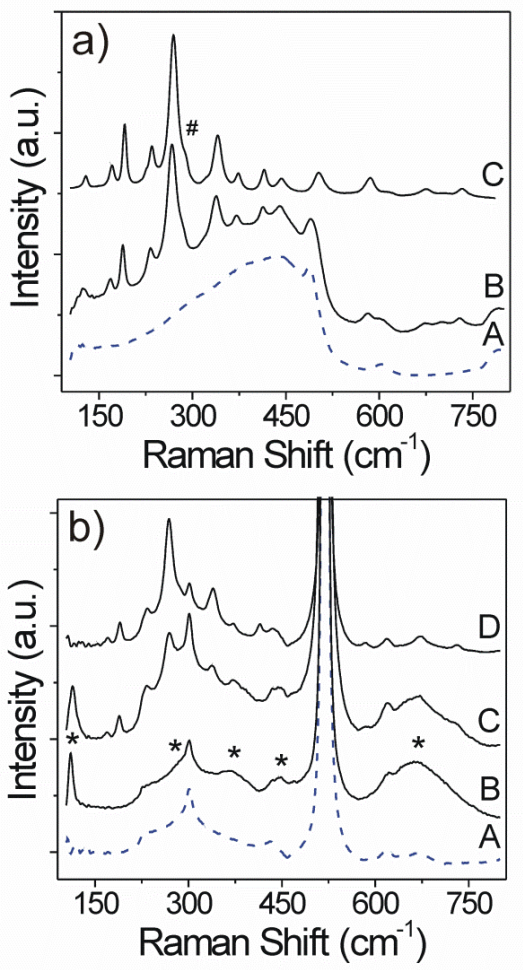

Figure 9. (a) Raman spectra obtained on a bare quartz glass slide (A), a KLE-templated YIG thin film on quartz heated to 900 °C (B) and non-templated YIG powder material heated to 1000 °C (C). The hash indicates a band that is not predicted by group theory. (b) Raman spectra for both a partially oxidized Si(100) wafer (A) and a KLE-templated YIG thin film on Si(100) heated to 800 °C (B), 850 °C (C) and 900 °C (D). Bands of metastable *h*-$YFeO_3$ are indicated by asterisks.

We also measured spectra as a function of annealing temperature to further support the crystallization pathway described in the section on XRD above. **Figure 9b** shows Raman data obtained on a KLE-templated thin film on a Si(100) wafer heated to 800 °C, 850 °C and 900 °C. The appearance of bands at ~111 cm^{-1} (strong), ~287 cm^{-1} (weak), ~370 cm^{-1} (medium/broad), ~448 cm^{-1} (medium) and ~660 cm^{-1} (strong/very broad) is indicative of the formation of *h*-$YFeO_3$.[81] However, the $Y_4Fe_2O_9$ phase could not be detected by Raman spectroscopy, the reason for which is not fully understood.

Nevertheless, the data in **Figure 9** are consistent with the result from XRD in that they show that single phase YIG is obtained after heating films to 900 °C.

Table 1. Raman band assignments and peak frequencies (cm^{-1}) for KLE-templated YIG thin films heated to 900 °C and single crystals of YIG.

	ref. [77] at 80 K	own study at 298 K
1	131 (T_{2g})	126 (T_{2g})
2	174 (T_{2g})	168 (T_{2g})
3	194 (T_{2g})	188 (T_{2g})
4	238 (T_{2g})	233 (T_{2g})
5	274 (E_{1g})	267
6	274 (T_{2g})	
	–	286 (#)
7	319 (E_{1g})	317
8	324 (T_{2g})	
9	346 (E_{1g})	339 (E_{1g})
10	378 (T_{2g})	371 (T_{2g})
11	416 (E_{1g})	413
12	419 (T_{2g})	
13	445 (T_{2g})	441 (T_{2g})
14	456 (E_{1g})	*
15	504 (A_{1g})	499 (A_{1g})
16	592 (T_{2g})	582 (T_{2g})
17	624 (E_{1g})	*
18	685 (E_{1g})	675
19	685 (T_{2g})	
20	692 (E_{1g})	
21	692 (T_{2g})	

22	704 (A_{1g})	701
23	711 (T_{2g})	
24	736 (A_{1g} or E_{1g})	729
25	736 (T_{2g})	

∗ superimposed, # unexpected

Lastly, XPS was used to obtain more insight into the chemical composition and the electronic bonding configuration. **Figure 10** shows both a survey spectrum and detail spectra of the Fe 2*p* and Y 3*d* core level regions of KLE-templated YIG thin films heated to 900 °C in air. Apart from a weak carbon C 1*s* peak, which we associate with adventitious hydrocarbon on the top surface, only iron, yttrium and oxygen core levels are observed. As expected, the Fe 2*p* spectrum in panel (b) contains an asymmetric doublet with distinct satellite peaks ~8 eV higher in binding energy than the main peaks, thereby indicating the Fe^{3+} oxidation state.[82] These data were fitted using spin-orbit splitting parameters with a relative peak area ratio of 1:2 for the $2p_{1/2}$ and $2p_{3/2}$ doublets, equal full width at half-maximum (FWHM) and with a peak separation of 13.45 eV. The component peaks at (723.68 ± 0.02) eV and (710.23 ± 0.02) eV for the $2p_{1/2}$ and $2p_{3/2}$ core levels, respectively, can be assigned to Fe^{3+} ions on tetrahedral 24(*d*) sites and those at (725.90 ± 0.02) eV and (712.45 ± 0.02) eV to Fe^{3+} ions on octahedral 16(*a*) sites.[83] By comparing the different peak areas, we find a ratio that is very close to the theoretical one of 3:2 for Fe^{3+} ions on tetrahedral and octahedral sites. Therefore, larger amounts of antisite defects can be ruled out. The Y 3*d* spectrum in panel (c) also contains a doublet due to spin-orbit splitting. However, these data can be fitted to two single peaks with binding energies of (158.34 ± 0.02) eV and (156.30 ± 0.02) eV for the $3d_{3/2}$ and $3d_{5/2}$ core levels, respectively.[83] In contrast, deconvolution of the O 1*s* spectrum (see **Figure S6**) indicates two different oxygen bonding states. The main peak centered at (529.26 ± 0.02) eV can be attributed to oxygen in YIG, while that at (531.05 ± 0.02) eV is likely due to surface hydroxyl groups.[83] Taken together, both the peak positions and separations are in agreement

with reported measured values for YIG and verify that the polymer-templated thin films are also well-defined on the atomic level.

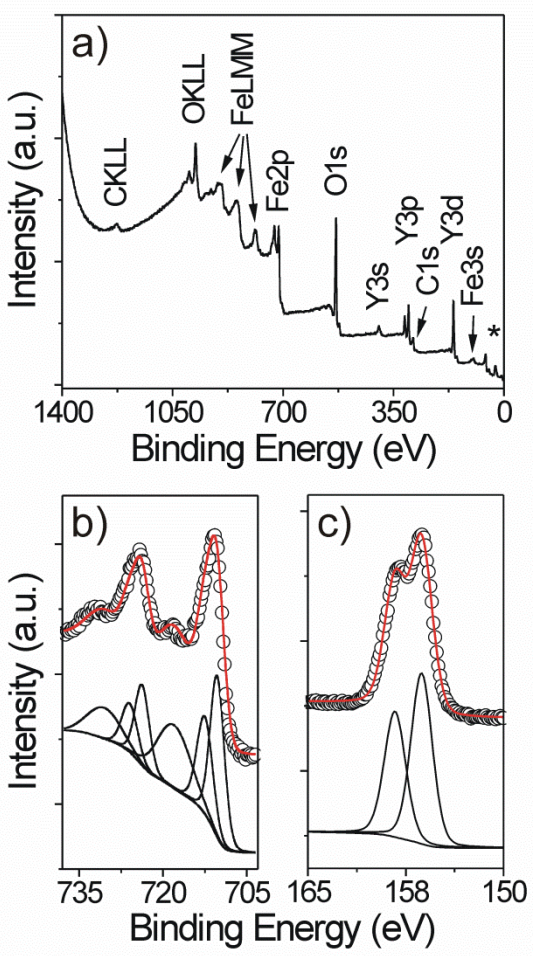

Figure 10. (a) XPS survey spectrum of KLE-templated YIG thin films heated to 900 °C in air. The Fe 3*p*, Y 4*s*, Y 4*p* and O 2*s* regions are indicated by an asterisk. (b, c) XPS detail spectra of the Fe 2*p* and Y 3*d* core levels. Black curves are fits to the data using mixed Gaussian-Lorentzian functions and red curves represent the sum of the peak fits. The Shirley method was applied to subtract backgrounds.

The magnetic properties of the KLE-templated YIG thin films heated to 900 °C were investigated by SQUID magnetometry for the temperature range 5–380 K in magnetic fields up to ±50 kOe. **Figure 11** shows typical in-plane zero-field-cooled (ZFC)/field-cooled (FC) curves measured in an applied field of 100 Oe. These experiments were made in heating runs and show how thermal fluctuations affect the dc magnetization, *M*. From the ZFC data, it can be seen that the mesoporous material starts off with a low

moment and that the magnetization continuously increases as the temperature is increased until a very broad maximum is reached at approx. 135 K. This maximum can be associated with the blocking temperature, T_B. We note that Sanchez *et al*. have shown that the single domain threshold grain size is ~190 nm and that the superparamagnetic threshold grain size at room temperature is ~35 nm.[84,85] It can also be seen that the ZFC and FC curves show large differences with $M_{ZFC} < M_{FC}$ below ~350 K. Overall, these features resemble the properties of cluster glasses and further suggest significant competition between short- and long-range magnetic interactions.[86,87] The FC data reveal a small peak at approx. 30 K which can be attributed to spin orientation rearrangement. The origin of the slight anomaly at ~300 K is not fully understood but might be associated with either some kind of magnetic domain rearrangement or a measurement artifact because the presence of impurity phases can be ruled out on the basis of the above results. From **Figure 11**, we estimate the Curie temperature, T_C, at which the material undergoes a ferromagnetic-paramagnetic phase transition to be 559 K. This value is in the range observed for nano- and microcrystalline YIG materials (550 K ≤ T_C ≤ 560 K).[85,88,89]

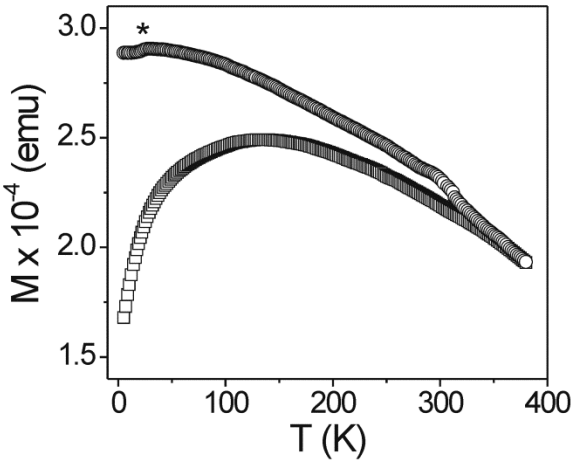

Figure 11. In-plane ZFC (□)/FC (○) curves measured in an applied field of 100 Oe. The asterisk indicates spin orientation rearrangement at low temperature.

Panels (a) and (b) of **Figure 12** show the reduced magnetization, M/M_{Sat}, as a function of field for both applied field directions at 5 K (i.e., in-plane and out-of-plane $M/M_{Sat}(H)$ loops with the external

magnetic field parallel and perpendicular to the plane of the film, respectively). It should be noted that the diamagnetic susceptibility (~1.5×10^{-7} emu·Oe^{-1}·g^{-1}) of the partially oxidized Si(100) wafers used as substrates in this work was subtracted from the overall response. As can be seen in **Figure 12,** the mesoporous material shows single phase magnetic behavior and further low-temperature behavior very similar to that of bulk films with a thickness equal to or greater than 50 nm.[89,90] In addition, the hysteresis loops indicate that the magnetic easy axis lies parallel to the plane of the substrate – the in-plane saturation field is significantly lower – as often observed for thin films due to shape anisotropy. Furthermore, we find that the in-plane coercivity (~68 Oe) is smaller than that in the out-of-plane direction (~98 Oe) and that the out-of-plane loop is more skewed, which points to different demagnetizing interactions and, perhaps, also to a different magnetization reversal process (i.e., domain wall displacement versus coherent rotation and domain wall motion). The cause of the magnetic anisotropy behavior has not been ascertained, though we believe it is due in part to strain anisotropy. Recently, we have shown for KLE-templated $CoFe_2O_4$ thin films that the unidirectional volume contraction during network condensation and crystallization generates in-plane tensile (expansive) strain which results in anisotropy.[91] The reason for this is that such thin films have only one free direction because they are bound to the substrate. This means that flexing of the pore cavities to accommodate the volume changes cannot take place in-plane but only in the out-of-plane direction (see section on GISAXS above). Consequently, the samples are under tension in the plane of the substrate after thermal treatment. Since the mesoporous YIG thin films undergo large unidirectional volume contraction (> 70%), as can be seen in **Figure 4**, the presence of strain in the garnet lattice is very likely. Overall, apart from the anisotropy, the KLE-templated YIG thin films studied here show soft magnetic-like characteristics somewhat similar to those observed in the bulk.

Panels (c) and (d) of **Figure 12** display in-plane $M(H)$ loops at different temperatures of 5 K, 100 K, 260 K and 380 K. As is evident, the magnetization is saturated above ~15 kOe at any of the temperatures and the coercivity decreases to ~10 Oe at 380 K. In contrast to sub 20 nm diameter particles, which show essentially zero coercivity at room temperature, in agreement with the

superparamagnetic threshold grain size estimated by Sanchez *et al.*,[84,85] the KLE-templated YIG thin films still reveal a small, yet measurable coercivity of 12-13 Oe. At this point, we believe that the weak ferrimagnetism is a direct result of the unique coupling of the nanocrystalline grains in the pore-solid architecture, even though 3D coupling typically leads to strong demagnetizing effects due to antiferromagnetic interactions.

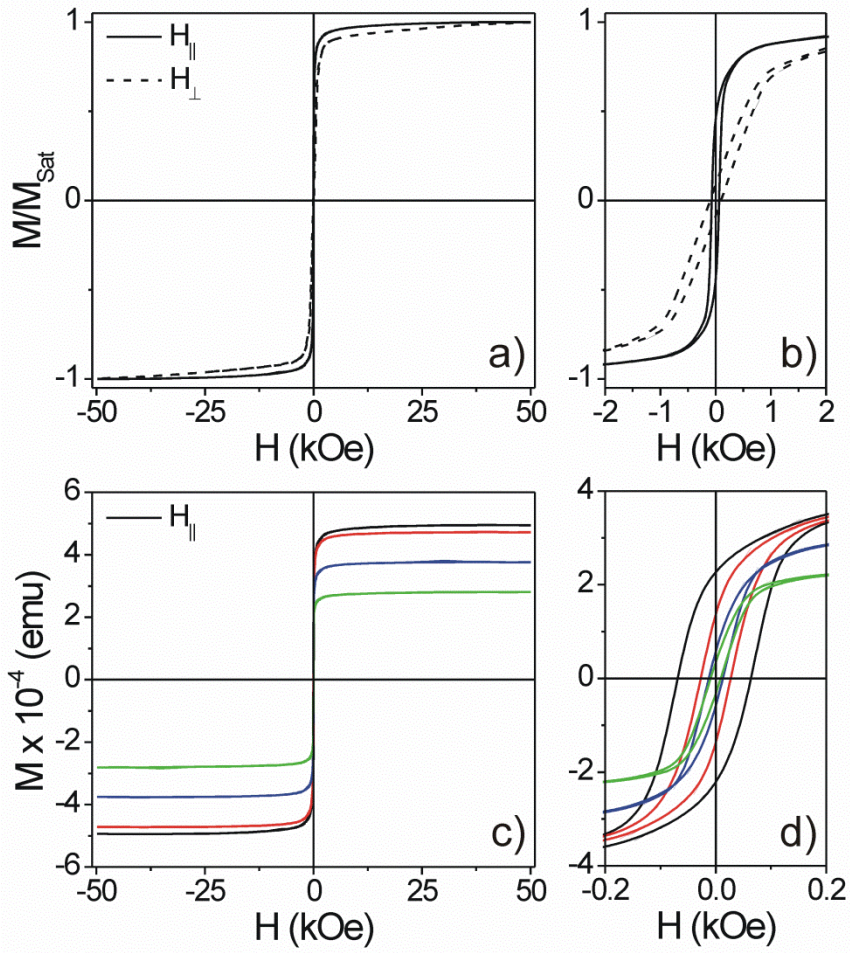

Figure 12. (a) In-plane and out-of-plane hysteresis curves at 5 K. (b) Hysteresis loops in the field range of ±2 kOe. (c) In-plane hysteresis curves at 5 K (black), 100 K (red), 260 K (blue) and 380 K (green). (d) Hysteresis loops in the field range of ±0.2 kOe showing that the coercive fields decrease as the temperature is increased from 5 k to 380 K.

To better characterize the magnetization behavior, the isothermal in-plane $M(H)$ curves were converted into Arrott plots (H/M versus M^2)[92] and the results are shown in panel (a) of **Figure 13**. This

method is based on the Landau theory of phase transitions and is widely used to accurately determine T_C. From the data, it is apparent that the mesoporous material in fact shows ferrimagnetic behavior in the temperature range 5–380 K. Also, the spontaneous magnetization, $M_S(T)$, can be determined through a linear extrapolation of the high field magnetization data, as indicated by the dashed lines in panel (a). The intercept of these extrapolations with the abscissa yields $M_S(T)$. Panel (b) of **Figure 13** shows M_S as a function of $T^{3/2}$. It can be clearly seen that the magnetization suppression behavior (due to the thermal excitation of spin waves) can be well described by Bloch's law[93], $M_S(T) = M_S(0)(1-B\cdot T^{3/2})$, in which $M_S(0)$ is the magnetization value at 0 K and B represents the spin wave parameter[94] ($B = 5.905\times10^{-5}$ $K^{-3/2}$). In summary, this means that within the magnon band structure, the magnetic moment varies as $T^{3/2}$ (over a broad temperature range) for localized magnetic moment systems, in agreement with Bloch's theoretical prediction for a 3D Heisenberg-type ferromagnet.[95] Lastly, we note that the other nanocrystalline rare-earth iron garnets synthesized also show room temperature ferrimagnetic ordering which, considering the high thermal stability of the pore-solid architectures, makes all these materials particularly interesting for host/guest thin film applications. It is envisioned that by filling the pore cavities using such methods as incipient wetness impregnation or sputtering, novel exchange coupled nanocomposite magnets and other multiphase materials with unprecedented properties can be produced.

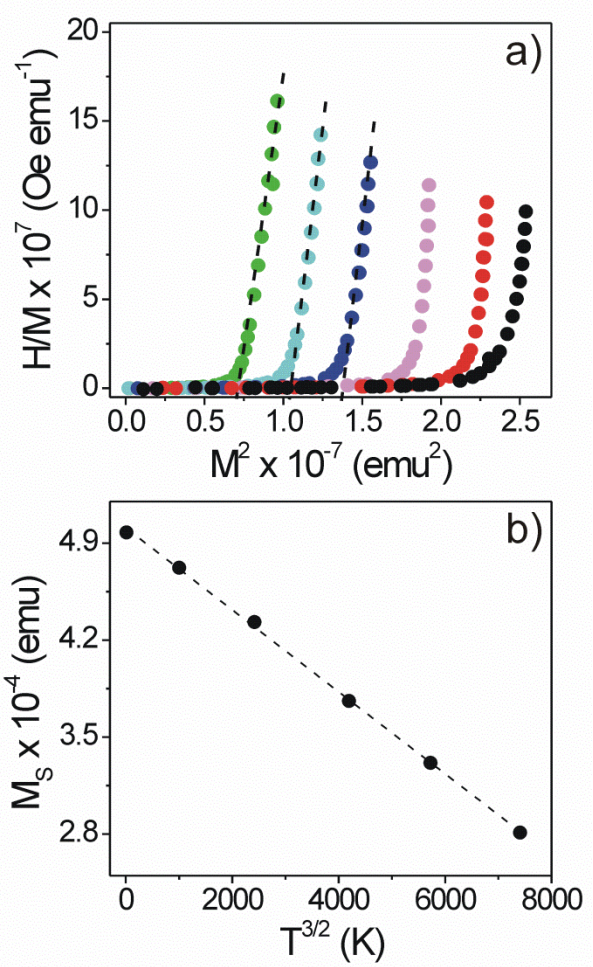

Figure 13. (a) M/H versus M^2 (Arrott plots) at temperatures of 5 K (black), 100 K (red), 180 K (pink), 260 K (blue), 320 K (cyan) and 380 K (green). (b) M_S versus $T^{3/2}$. The dashed lines in panel (a) indicate the linear fitting to the high field magnetization data to determine $M_S(T)$. The dashed line in panel (b) is a fit to Bloch's $T^{3/2}$ law.

Conclusion

Ordered mesoporous thin films of $Y_3Fe_5O_{12}$ have been successfully synthesized for the first time by facile polymer templating of hydrated nitrate salt precursors. Despite solid-solid conversions throughout the course of crystallization – $Y_3Fe_5O_{12}$ *via* $Y_4Fe_2O_9$ and *h*-$YFeO_3$ – the cubic architecture with 16 nm diameter pore cavities is retained when the garnet phase is achieved. Characterization of the morphology and the microstructure using various state-of-the-art techniques indicates that the polymer-

templated $Y_3Fe_5O_{12}$ thin films studied in this work are single phase after heating to 900 °C and that the presence of larger amounts of defects both on the nano- and microscale and on the atomic level can be ruled out. SQUID magnetometry studies further establish the high quality of the room temperature magnetic $Y_3Fe_5O_{12}$ thin films with overall soft magnetic-like characteristics. Furthermore, the method employed here is shown to be extendable to other rare-earth iron garnets, including $Gd_3Fe_5O_{12}$, $Tb_3Fe_5O_{12}$ and $Dy_3Fe_5O_{12}$, with similar pore structure and nanocrystalline walls, which paves the way for exploring the ferroic properties of a new class of interface-controlled materials.

Associated Content

Supporting Information. Additional data from UV-vis spectroscopy, XRD, XPS, SAXS and SEM and TEM imaging. This material is available free of charge via the Internet at http://pubs.acs.org.

Author Information

Corresponding Author

*E-mail: torsten.brezesinski@kit.edu. Phone: +49 721 608-28827.

*E-mail: christian.suchomski@kit.edu. Phone: +49 641 99-34592.

Author Contributions

C.S., C.T.S. and J.P.A.: experimental work and data analysis. T.B.: project planning and data analysis. The manuscript was written by C.S. and T.B. All authors have given approval to the final version of the manuscript.

Funding Sources

Financial support by the German Research Foundation (grant no. BR 3499/3-1) is gratefully acknowledged. C.T.S. is grateful to FCT for a post-doctoral grant (SFRH/BPD/82010/2011).

Notes

The authors declare no competing financial interest.

Acknowledgement

The authors thank Jan Haetge and Thomas Leichtweiss for assistance in materials characterization and HASYLAB at DESY for beamtime.

References

[1] Gunther, L. *Phys. World* **1990,** *3*, 28-34.
[2] Gupta, A. K.; Gupta, M. *Biomaterials* **2005,** *26*, 3995-4021.
[3] Hyeon, T. *Chem. Commun.* **2003**, 927-934.
[4] Leslie-Pelecky, D. L.; Rieke, R. D. *Chem. Mater.* **1996,** *8*, 1770-1783.
[5] Batlle, X.; Labarta, A. *J. Phys. D Appl. Phys.* **2002,** *35*, R15-R42.
[6] Lu, A. H.; Salabas, E. L.; Schuth, F. *Angew. Chem. Int. Edit.* **2007,** *46*, 1222-1244.
[7] Gubin, S. P.; Koksharov, Y. A.; Khomutov, G. B.; Yurkov, G. Y. *Usp. Khim.* **2005,** *74*, 539-574.
[8] Nogues, J.; Sort, J.; Langlais, V.; Skumryev, V.; Surinach, S.; Munoz, J. S.; Baro, M. D. *Phys. Rep.* **2005,** *422*, 65-117.
[9] Eisenmenger, J.; Schuller, I. K. *Nat. Mater.* **2003,** *2*, 437-438.
[10] Jeong, U.; Teng, X. W.; Wang, Y.; Yang, H.; Xia, Y. N. *Adv. Mater.* **2007,** *19*, 33-60.
[11] Dillon, J. F. *J. Appl. Phys.* **1958,** *29*, 539-541.
[12] Serga, A. A.; Chumak, A. V.; Hillebrands, B. *J. Phys. D Appl. Phys.* **2010,** *43*, 264002.
[13] Hansen, P.; Krumme, J. P. *Thin Solid Films* **1984,** *114*, 69-107.
[14] Pardavi-Horvath, M. *J. Magn. Magn. Mater.* **2000,** *215*, 171-183.
[15] Eppler, W. R.; Kryder, M. H. *J. Phys. Chem. Solids* **1995,** *56*, 1479-1490.
[16] Bertaut, F.; Forrat, F. *C.R. Hebd. Acad. Sci.* **1956,** *242*, 382-384.
[17] Geller, S.; Gilleo, M. A. *J. Phys. Chem. Solids* **1957,** *3*, 30-36.
[18] Sztaniszlav, A.; Sterk, E.; Fetter, L.; Farkasjahnke, M.; Labar, J. *J. Magn. Magn. Mater.* **1984,** *41*, 75-78.
[19] Fernandez-Garcia, L.; Suarez, M.; Menendez, J. L. *J. Alloy. Compd.* **2010,** *495*, 196-199.
[20] Ristic, M.; Nowik, I.; Popovic, S.; Felner, I.; Music, S. *Mater. Lett.* **2003,** *57*, 2584-2590.
[21] Vaqueiro, P.; Crosnier-Lopez, M. P.; Lopez-Quintela, M. A. *J. Solid State Chem.* **1996,** *126*, 161-168.
[22] Vaqueiro, P.; Lopez-Quintela, M. A. *Chem. Mater.* **1997,** *9*, 2836-2841.
[23] Todorovska, R.; Groudeva-Zotova, S.; Todorovsky, D.; Tzvetkov, G.; Stefanov, P. *J. Mater. Synth. Proces.* **2002,** *10*, 283-288.
[24] Vajargah, S. H.; Hosseini, H. R. M.; Nemati, Z. A. *J. Alloy. Compd.* **2007,** *430*, 339-343.
[25] Jafelicci, M.; Godoi, R. H. M. *J. Magn. Magn. Mater.* **2001,** *226*, 1421-1423.
[26] Lu, Y. F.; Ganguli, R.; Drewien, C. A.; Anderson, M. T.; Brinker, C. J.; Gong, W. L.; Guo, Y. X.; Soyez, H.; Dunn, B.; Huang, M. H.; Zink, J. I. *Nature* **1997,** *389*, 364-368.
[27] Brinker, C. J.; Lu, Y. F.; Sellinger, A.; Fan, H. Y. *Adv. Mater.* **1999,** *11*, 579-585.
[28] Grosso, D.; Cagnol, F.; Soler-Illia, G.; Crepaldi, E. L.; Amenitsch, H.; Brunet-Bruneau, A.; Bourgeois, A.; Sanchez, C. *Adv. Funct. Mater.* **2004,** *14*, 309-322.
[29] Yang, P. D.; Zhao, D. Y.; Margolese, D. I.; Chmelka, B. F.; Stucky, G. D. *Nature* **1998,** *396*, 152-155.

[30] Choi, S. Y.; Mamak, M.; Coombs, N.; Chopra, N.; Ozin, G. A. *Adv. Funct. Mater.* **2004,** *14*, 335-344.
[31] Grosso, D.; Boissiere, C.; Smarsly, B.; Brezesinski, T.; Pinna, N.; Albouy, P. A.; Amenitsch, H.; Antonietti, M.; Sanchez, C. *Nat. Mater.* **2004,** *3*, 787-792.
[32] Innocenzi, P.; Malfatti, L. *Chem. Soc. Rev.* **2013**, *42*, 4198-4216.
[33] Sanchez, C.; Boissiere, C.; Grosso, D.; Laberty, C.; Nicole, L. *Chem. Mater.* **2008,** *20*, 682-737.
[34] Ren, Y.; Ma, Z.; Bruce, P. G. *Chem. Soc. Rev.* **2012,** *41*, 4909-4927.
[35] Kresge, C. T.; Leonowicz, M. E.; Roth, W. J.; Vartuli, J. C.; Beck, J. S. *Nature* **1992,** *359*, 710-712.
[36] Ciesla, U.; Schuth, F. *Microporous Mesoporous Mat.* **1999,** *27*, 131-149.
[37] Corma, A.; Atienzar, P.; Garcia, H.; Chane-Ching, J. Y. *Nat. Mater.* **2004,** *3*, 394-397.
[38] Deshpande, A. S.; Pinna, N.; Smarsly, B.; Antonietti, M.; Niederberger, M. *Small* **2005,** *1*, 313-316.
[39] Rauda, I. E.; Buonsanti, R.; Saldarriaga-Lopez, L. C.; Benjauthrit, K.; Schelhas, L. T.; Stefik, M.; Augustyn, V.; Ko, J.; Dunn, B.; Wiesner, U.; Milliron, D. J.; Tolbert, S. H. *ACS Nano* **2012,** *6*, 6386-6399.
[40] Thomas, A.; Schlaad, H.; Smarsly, B.; Antonietti, M. *Langmuir* **2003,** *19*, 4455-4459.
[41] Brezesinski, T.; Antonietti, M.; Smarsly, B. M. *Adv. Mater.* **2007,** *19*, 1074-1078.
[42] Suchomski, C.; Reitz, C.; Brezesinski, K.; Tavares de Sousa, C.; Rohnke, M.; Iimura, K.; Esteves de Araujo, J. P.; Brezesinski, T. *Chem. Mater.* **2012**, *24*, 155-165.
[43] Haetge, J.; Suchomski, C.; Brezesinski, T. *Inorg. Chem.* **2010,** *49*, 11619-11626.
[44] Schlaad, H.; Kukula, H.; Rudloff, J.; Below, I. *Macromolecules* **2001**, *34*, 4302-4304.
[45] Haetge, J.; Djerdj, I.; Brezesinski, T. *Chem. Commun.* **2012,** *48*, 6726-6728.
[46] Wieczorek-Ciurowa, K.; Kozak, A. J. *Therm. Anal. Calorim.* **1999,** *58*, 647-651.
[47] Hussein, G. A. M. *Thermochim. Acta* **1994,** *244*, 139-151.
[48] Schildermans, I.; Mullens, J.; Yperman, J.; Franco, D.; Vanpoucke, L. C. *Thermochim. Acta* **1994,** *231*, 185-192.
[49] Gobichon, A. E.; Auffredic, J. P.; Louer, D. *Solid State Ion.* **1996,** *93*, 51-64.
[50] Bonnet, M.; Delapalme, A.; Fuess, H.; Thomas, M. *Acta Crystallogr. Sect. B-Struct. Sci.* **1975,** *31*, 2233-2240.
[51] Wemple, S. H.; Blank, S. L.; Seman, J. A.; Biolsi, W. A. *Phys. Rev. B* **1974,** *9*, 2134-2144.
[52] Scott, G. B.; Lacklison, D. E.; Page, J. L. *Phys. Rev. B* **1974,** *10*, 971-986.
[53] Ching, W. Y.; Gu, Z. Q.; Xu, Y. N. *J. Appl. Phys.* **2001,** *89*, 6883-6885.
[54] Pisarev, R. V.; Moskvin, A. S.; Kalashnikova, A. M.; Rasing, T. *Phys. Rev. B* **2009,** *79*.
[55] Jung, J. H.; Matsubara, M.; Arima, T.; He, J. P.; Kaneko, Y.; Tokura, Y. *Phys. Rev. Lett.* **2004,** *93*.
[56] Sherman, D. M. *Phys. Chem. Miner.* **1985,** *12*, 161-175.
[57] Balzarotti, A.; Picozzi, P.; Ricchiuto, A.; Santucci, S. *J. Phys. C Solid State* **1979,** *12*, 5233-5243.
[58] Scott, G. B.; Page, J. L. *Phys. Status Solidi B* **1977,** *79*, 203-213.
[59] Makhnev, A. A.; Gizhevskii, B. A.; Nomerovannaya, L. V. *Jetp Lett.* **2010,** *91*, 79-82.
[60] Shablaev, S. I.; Pisarev, R. V. *Jetp Lett.* **1987,** *45*, 626-630.
[61] Larsen, P. K.; Metselaar, R. *J. Solid State Chem.* **1975,** *12*, 253-258.
[62] Metselaar, R.; Larsen, P. K. *Solid State Commun.* **1974,** *15*, 291-294.
[63] Vanhook, H. J. *J. Am. Ceram. Soc.* **1961,** *44*, 208-214.
[64] Vanhook, H. J. *J. Am. Ceram. Soc.* **1962,** *45*, 162-165.
[65] Buscaglia, V.; Caracciolo, F.; Bottino, C.; Leoni, M.; Nanni, P. *Acta Mater.* **1997,** *45*, 1213-1224.
[66] Yamaguchi, O.; Takemura, H.; Yamashita, M.; Hayashida, A. *J. Electrochem. Soc.* **1991,** *138*, 1492-1494.

[67] Nagashio, K.; Kuribayashi, K.; Kumar, M. S. V.; Niwata, K.; Hibiya, T.; Mizuno, A.; Watanabe, M.; Katayama, Y. *Appl. Phys. Lett.* **2006,** *89*, 241923.
[68] Li, J.; Singh, U. G.; Schladt, T. D.; Stalick, J. K.; Scott, S. L.; Seshadri, R. *Chem. Mater.* **2008,** *20*, 6567-6576.
[69] Popova, V. F.; Petrosyan, A. G.; Tugova, E. A.; Romanov, D. P.; Gusarov, V. V. *Russ. J. Inorg. Chem.* **2009,** *54*, 624-629.
[70] Liu, F. S.; Liu, Q. L.; Liang, J. K.; Song, G. B.; Luo, J.; Yang, L. T.; Zhang, Y.; Rao, G. H. *J. Alloy. Compd.* **2004,** *381*, 26-31.
[71] Roof, I. P.; Smith, M. D.; zur Loye, H. C. *Solid State Sci.* **2010,** *12*, 1211-1214.
[72] Liu, F. S.; Liu, Q. L.; Liang, J. K.; Yang, L. T.; Song, G. B.; Luo, J.; Rao, G. H. *J. Solid State Chem.* **2004,** *177*, 1796-1802.
[73] Liu, F. S.; Liu, Q. L.; Liang, J. K.; Luo, J.; Yang, L. T.; Song, G. B.; Zhang, Y.; Wang, L. X.; Yao, J. N.; Rao, G. H. *J. Alloy. Compd.* **2006,** *425*, 278-283.
[74] Iida, Y.; Towata, A.; Tsugoshi, T.; Furukawa, M. *Vib. Spectrosc.* **1999,** *19*, 399-405.
[75] Sim, S. M.; Keller, K. A.; Mah, T. I. *J. Mater. Sci.* **2000,** *35*, 713-717.
[76] Hurrell, J. P.; Porto, S. P. S.; Chang, I. F.; Mitra, S. S.; Bauman, R. P. *Phys. Rev.* **1968,** *173*, 851-856.
[77] Song, J. J.; Klein, P. B.; Wadsack, R. L.; Selders, M.; Mroczkowski, S.; Chang, R. K. *J. Opt. Soc. Am.* **1973,** *63*, 1135-1140.
[78] Grunberg, P.; Koningstein, J. A.; van Uitert, L. G. *J. Opt. Soc. Am.* **1971** *61*, 1613-1617.
[79] Novak, P.; Englich, J.; Stepankova, H.; Kohout, J.; Lutgemeier, H.; Wagner, K.; Tolksdorf, W. *Phys. Rev. Lett.* **1995,** *75*, 545-548.
[80] Dong, J.; Lu, K. *Phys. Rev. B* **1991,** *43*, 8808-8821.
[81] Wu, L.; Yu, J. C.; Zhang, L.; Wang, X.; Li, S. *J. Solid State Chem.* **2004,** *177*, 3666-3674.
[82] Mullet, M.; Guillemin, Y.; Ruby, C. *J. Solid State Chem.* **2008,** *181*, 81-89.
[83] Simsa, Z.; Zemek, J. *Czech. J. Phys.* **1990,** *40*, 1274-1282.
[84] Sanchez, R. D.; Rivas, J.; Vaqueiro, P.; Lopez-Quintela, M. A.; Caeiro, D. *J. Magn. Magn. Mater.* **2002,** *247*, 92-98.
[85] Sanchez, R. D.; Ramos, C. A.; Rivas, J.; Vaqueiro, P.; Lopez-Quintela, M. A. *Physica B* **2004,** *354*, 104-107.
[86] Kumar, P. S. A.; Joy, P. A.; Date, S. K. *J. Phys.-Condens. Mat.* **1998,** *10*, L487-L493.
[87] Marcano, N.; Sal, J. C. G.; Espeso, J. I.; Barquin, L. F.; Paulsen, C. *Phys. Rev. B* **2007,** *76*.
[88] Anderson, E. E. *Phys. Rev.* **1964,** *134*, 1581-1585.
[89] Krockenberger, Y.; Yun, K. S.; Hatano, T.; Arisawa, S.; Kawasaki, M.; Tokura, Y. *J. Appl. Phys.* **2009,** *106*, 123911.
[90] Popova, E.; Keller, N.; Gendron, F.; Guyot, M.; Brianso, M. C.; Dumond, Y.; Tessier, M. *J. Appl. Phys.* **2001,** *90*, 1422-1428.
[91] Quickel, T. E.; Le, V. H.; Brezesinski, T.; Tolbert, S. H. *Nano Lett.* **2010,** *10*, 2982-2988.
[92] Arrott, A. *Phys. Rev.* **1957,** *108*, 1394-1396.
[93] Bloch, F. *Z. Physik* **1930,** *61*, 206-219.
[94] Sperl, M.; Singh, A.; Wurstbauer, U.; Das, S. K.; Sharma, A.; Hirmer, M.; Nolting, W.; Back, C. H.; Wegscheider, W.; Bayreuther, G. *Phys. Rev. B* **2008,** *77*.
[95] Della Torre, E.; Bennett, L. H.; Watson, R. E. *Phys. Rev. Lett.* **2005,** *94*, 147210.

Table of Contents Graphic